

# Supporting Information

## **From Milliseconds to Minutes: Melittin Self-Assembly from Concerted Non-Equilibrium Pressure-Jump and Equilibrium Relaxation NMR**

Martin D. Gelenter, Wai-Ming Yau, Philip A. Anfinrud, and Ad Bax\*

Laboratory of Chemical Physics, NIDDK, National Institutes of Health, Bethesda, MD 20892

\*Corresponding author: Ad Bax: [bax@nih.gov](mailto:bax@nih.gov)

## Materials & Methods

### I. Peptide Synthesis

Synthetic melittin (amino acid sequence H<sub>2</sub>N-GIGAVLKVLTTGLPALISWIKRKRQQ-NH<sub>2</sub>) was synthesized with standard Fmoc solid-phase peptide synthesis and purified as previously described.<sup>1</sup> Samples used to study P14 *cis-trans* isomerization were <sup>13</sup>C and <sup>15</sup>N labeled for residues L13 and A15. Isotopically labeled residues were double coupled using a three-fold excess, while natural abundance residues were single coupled with a five-fold excess.

### II. Recombinant Expression and Chemical Amidation of <sup>2</sup>H,<sup>13</sup>C,<sup>15</sup>N-Labeled Melittin

Recombinant expression and chemical amidation to produce triply labeled native melittin was done as previously described.<sup>2</sup> Briefly, <sup>2</sup>H,<sup>13</sup>C,<sup>15</sup>N-labeled GST-melittin-COOH was expressed in M9 minimal media containing 99.9% D<sub>2</sub>O (Sigma-Aldrich, St. Louis, MO), 97-98% <sup>13</sup>C,<sup>2</sup>H-labeled glucose (Cambridge Isotopes Laboratories, Tewksbury, MA), and 99% <sup>15</sup>N-labeled NH<sub>4</sub>Cl (Cambridge Isotopes Laboratories, Tewksbury, MA). Prior to cleavage with Tobacco Etch Virus (TEV) protease, GST-melittin-COOH was purified with a GStrap HP GST affinity chromatography column (Cytiva, Marlborough, MA) and dialyzed into buffer suitable for TEV protease cleavage. After a reverse GST affinity column to remove the cleaved GST, the <sup>2</sup>H,<sup>13</sup>C,<sup>15</sup>N-labeled melittin-COOH was purified via high performance liquid chromatography (HPLC) (Phenomenex, Torrance, CA; Agilent, Santa Clara, CA) and lyophilized.

Melittin-COOH was then Boc-protected using di-*tert*-butyl decarbonate (Boc<sub>2</sub>O) in the presence of *N,N*-diisopropylethylamine (DIPEA) with *N,N*-dimethylformamide (DMF) as the organic solvent. Rather than HPLC purifying the Boc-melittin-COOH as had been done previously,<sup>2</sup> once the Boc protection reaction had reached completion, 1-[Bis(dimethylamino)methylene]-1H-1,2,3-triazolo[4,5-*b*]pyridinium 3-oxide hexafluorophosphate (HATU), <sup>15</sup>NH<sub>4</sub>Cl, and DIPEA were added directly to the reaction mixture, at the same concentrations as previously reported,<sup>2</sup> to amidate the C terminus. This “one pot” amidation strategy resulted in the same yield as the previous method but cut down on sample loss from extraneous HPLC purification steps and saved two days in preparation time by the elimination of one HPLC and lyophilization step. Following the amidation reaction, the Boc protecting groups were deprotected in an ice-cold solution of 95:5 TFA:DMF for one hour prior to a final HPLC purification step. The ion-exchange purification step described in our previous publication<sup>2</sup> to separate unreacted melittin-COOH from amidated melittin-CONH<sub>2</sub> was omitted in this study to increase yields, as the unreacted melittin-COOH only amounted to a ~3% impurity and did not show evidence for interacting with and changing the kinetics or structure of the melittin-CONH<sub>2</sub> tetramer.

### III. NMR Spectroscopy

All NMR samples were prepared in 25 mM sodium phosphate buffer, pH 7.0, with 50 mM NaCl, 500 μM benzamidine, 100 μM sodium trimethylsilylpropanesulfonate (DSS), and 3% D<sub>2</sub>O. Samples were spiked with 100 μM <sup>15</sup>N-labeled tryptophan for quantification purposes. Prior to running NMR experiments all samples were dialyzed against NMR buffer using a Slide-A-Lyzer dialysis cassette with a 2-kDa molecular weight cutoff (Thermo Fisher, Waltham, MA) to equilibrate the pH and remove remaining TFA that had acted as a counter-ion after lyophilization.

Peptide concentrations were measured via melittin's absorbance at 280 nm and confirmed via high pressure 1D  $^1\text{H}$  spectra and 2D  $^{15}\text{N}$ - $^1\text{H}$  HSQC spectra.

Unless stated otherwise, NMR experiments were conducted on a 600-MHz Bruker Avance Neo spectrometer equipped with a 5-mm cryoprobe with a z-axis gradient at a setpoint temperature of 288 K. A total of 215  $\mu\text{L}$  of sample was loaded into a zirconia high pressure cell with an outer diameter of 5 mm and inner diameter of 2.6 mm, rated for up to 3 kbar of hydrostatic pressure (Daedalus Innovations, Ashton, PA). Mineral spirits (Sigma-Aldrich, Saint Louis, MO) were then added to the top of the sample and used as the hydraulic fluid in subsequent pressure-jump experiments. Pressure-jump experiments utilized a home-built apparatus described previously.<sup>3</sup>

$^{15}\text{N}$  TROSY  $R_2$  values were measured (Figure 2f) using a TROSY experiment with water flip-back pulses in which the delays for a  $^{15}\text{N}$  echo prior to the indirect dimension chemical shift encoding were varied from 1 ms to 101 ms with five total increments (1, 21, 41, 61, and 101 ms). Due to the line narrowing afforded by TROSY experiments,<sup>4</sup> and subsequent slower  $R_2$ 's, for a deuterated 12 kDa tetramer, these  $R_2$  experiments set tighter restraints on the  $R_{ex}$  contribution to the measured effective  $R_2$  than a traditional HSQC  $^{15}\text{N}$   $R_2$  measurement.<sup>5</sup>

All NMR data were processed with NMRpipe.<sup>6</sup> Both NMRpipe and Matlab were used in data analysis and parameter fitting.

#### ***IV. Proline cis-trans Isomerization Pressure-Jump NMR Experiments***

The kinetics of P14 *cis-trans* isomerization was measured using both a single pressure drop, with repeated HSQCs collected after the pressure drop,<sup>7</sup> and with a double jump experiment in which the pressure is dropped for a variable delay,  $\tau_{\text{fold}}$ , before being jumped back to high pressure for a  $^{15}\text{N}$ - $^1\text{H}$  HSQC readout. The single jump experiment has superior sensitivity, as the P14 *cis* and *trans* populations do not need to be re-equilibrated between each successive HSQC. However, these experiments suffer from a lack of temporal resolution: there is a dead time of thirty seconds after the pressure drop, needed for temperature gradients associated with adiabatic expansion of the solvent to dissipate, which is a requirement for high resolution and good line shapes, and each HSQC takes at least two minutes. The double jump experiment allows for arbitrarily short  $\tau_{\text{fold}}$  delays. All proline *cis-trans* isomerization kinetics data in the main text and Supporting Information were measured on a 2.0 mM sample of synthetic melittin with  $^{13}\text{C}$  and  $^{15}\text{N}$  labeling for residues L13 and A15 (LA-melittin). The P14 *cis* experiments on a 1.0 mM sample did not show different P14 *cis-trans* isomerization kinetics from the 2.0 mM sample; there also was no concentration dependence observed for P14 *cis-trans* isomerization in melittin.

The single pressure drop P14 *cis-trans* isomerization experiments (Figure 1c, Figure S1a-c, Figure S2a,b) start with a pressure drop from 2.25 kbar to atmospheric pressure followed by a 30 s deadtime to allow for sample equilibration and to re-lock the  $\text{D}_2\text{O}$  signal. Following this 30 s dead time, a series of short  $^{15}\text{N}$ - $^1\text{H}$  HSQCs were collected to track the change in the P14 *cis* population over time. These short HSQCs start with 8 dummy scans followed by two-scan FIDs for data acquisition for a total of two minutes per HSQC. Sweep widths of 15.15 and 10.0 ppm were used for the direct  $^1\text{H}$  dimension and the indirect  $^{15}\text{N}$  dimension, respectively. The direct dimension was acquired for 84.5 ms, while the indirect dimension was evolved for a total of 57.5 ms. A short recycle delay of 0.62 s was used to make the experimental time relatively short. This

short recycle delay did not result in significant signal-to-noise reductions due to incomplete  $T_1$  relaxation.

The double jump experiment (Figure 1d, Figure S1d-f, Figure S2c,d) used for measuring P14 *cis-trans* isomerization kinetics begins with an equilibration period at high pressure (2.25 kbar) that is sufficiently long to equilibrate the P14 *cis* and *trans* populations. Following this preparation period, the pressure is dropped for a delay,  $\tau_{\text{fold}}$ , before being jumped back up to 2.25 kbar. After a 500-ms delay to allow the peptide with P14 in the *trans* conformation to fold and oligomerize, a short HSQC is collected with one scan per FID and a recycle delay of 500 ms for a total of 26 seconds. Sweep widths of 15.15 and 10.0 ppm were used for the direct  $^1\text{H}$  dimension and the indirect  $^{15}\text{N}$  dimension, respectively. The direct dimension was acquired for 84.5 ms, while the indirect dimension was evolved for a total of 41.1 ms. After the HSQC was collected, the sample was re-equilibrated at 2.25 kbar before repeating this sequence a second time. The second HSQC also only consists of 1 scan per FID; these two HSQCs are phase cycled such that when their FIDs are added together, it yields the spectrum that would be observed for a 2-scan phase-cycled HSQC. Four sets of these experiments were collected for each  $\tau_{\text{fold}}$  delay and added together so that each time point is equivalent to an HSQC collected with 8 scans per FID.  $\tau_{\text{fold}}$  delays ranging from 2 to 340 s were used at 288 K and 2 to 1800 s at 278 K. The peak intensities corresponding to the L13 and A15 residues with P14 in the *cis* conformation were tracked as the  $\tau_{\text{fold}}$  delay was varied.

### ***V. Oligomerization & Protein Folding Pressure-Jump NMR Experiments***

Population weighted average  $^{15}\text{N}$  chemical shifts were measured in a stroboscopic fashion using a pseudo-3D experiment (Figure 2a, Figure S4) on a 600 MHz spectrometer at four different  $^2\text{H}$ ,  $^{13}\text{C}$ ,  $^{15}\text{N}$ -labeled melittin concentrations: 0.25 mM, 0.5 mM, 0.8 mM, and 1.1 mM (Figure 2b-e, Figure S6).<sup>7,8</sup> After a  $\sim 10$ s preparation period at high pressure, where the peptide is equilibrated in the pressure-denatured state, a refocused INEPT generates in-phase  $N_z$  magnetization prior to a pressure drop to atmospheric pressure. Following the pressure drop, a variable folding delay,  $\tau_{\text{fold}}$ , precedes the stroboscopic chemical shift encoding. The pressure is then jumped back up to 2.25 kbar and the peptide is allowed to denature for a 350 ms “unfold & dissociate” period prior to evolving the indirect  $^{15}\text{N}$  dimension and INEPT transfer back to  $^1\text{H}$  for detection.

The stroboscopic chemical shift evolution period,  $\kappa$ , of the 0.25-mM sample was set to 1.125 ms, resulting in a bandwidth of 889 Hz (14.6 ppm at 600 MHz), while all other concentrations utilized a  $\kappa$  value of 0.5-ms, corresponding to a 2-kHz bandwidth (32.9 ppm). Data were collected with spectral widths of 15.15 ppm and 20.0 ppm for the direct  $^1\text{H}$  dimension and indirect  $^{15}\text{N}$  dimension, respectively. The direct dimension was acquired for 113 ms, while the indirect dimension evolved for a total of 82 ms. FIDs were collected in an interleaved manner such that first the delay between the pressure drop and stroboscopic chemical shift evolution,  $\tau_{\text{fold}}$ , was varied while the stroboscopic chemical shift was cosine-modulated due to the population-weighted average  $^{15}\text{N}$  chemical shift. Then, the sine-modulated signal was measured by changing the phase of the first pulse in the pseudo dimension by  $90^\circ$ . Finally, the indirect  $^{15}\text{N}$  dimension was evolved, using Rance-Kay gradient selection.<sup>9</sup>

For the 1.1-mM sample, 15  $\tau_{\text{fold}}$  time points were used (2, 5, 10, 15, 20, 25, 30, 40, 50, 60, 80, 100, 150, 200, and 250 ms), for a total experimental time of 16.7 hours. For the 0.8 mM sample,

15  $\tau_{\text{fold}}$  time points were used (2, 5, 10, 15, 20, 30, 40, 60, 80, 100, 150, 200, 250, 300, and 350 ms), for a total experimental time of 16.9 hours. For the 0.25- and 0.5-mM samples, 10  $\tau_{\text{fold}}$  time points were used (2, 5, 10, 20, 40, 80, 160, 240, 320, and 400 ms), for a total experimental time of 20.3 hours. All experiments were run in a double jump fashion, in which after the folding period, the pressure was jumped back to high pressure for the HSQC readout. At high pressure melittin exists as an intrinsically disordered protein, giving it favorable relaxation times and linewidths for detection via a  $^{15}\text{N}$ - $^1\text{H}$  HSQC experiment.

## VI. $^{15}\text{N}$ CPMG Relaxation Dispersion Experiments

$^{15}\text{N}$  (Carr-Purcell-Meiboom-Gill) CPMG relaxation dispersion experiments were conducted at 600 MHz utilizing  $^1\text{H}$  continuous-wave (CW) decoupling during the CPMG relaxation block to measure relaxation of in-phase  $^{15}\text{N}$  coherences (Figure 2g-j, Figure S10).<sup>10</sup> The total peptide concentrations was 1.0 mM, and consisted of a 1:3 ratio of  $^2\text{H}$ ,  $^{13}\text{C}$ ,  $^{15}\text{N}$ -labeled:natural abundance melittin. The  $^1\text{H}$  CW decoupling field strength was set to be an integer multiple of the CPMG frequency; most data points used a 12-kHz field strength, while slightly lower CW field strengths were used for CPMG frequencies that are not factors of 12 kHz. Effective  $R_2$ 's were measured in a constant-time fashion, with the CPMG evolution period totaling 40 ms. In addition to a reference experiment, where the CPMG relaxation block was omitted, 17 CPMG frequencies were measured (25, 50, 75, 100, 125, 150, 200, 250, 300, 350, 400, 500, 600, 700, 800, 900, and 1000 Hz). Errors were propagated using the signal-to-noise as a measure of the standard error for each peak intensity. At the intermediate concentration used for these CPMG experiments, many residues show resolved resonances for both the unfolded monomer and the folded tetramer, so that exchange for both of these species can be probed simultaneously.

## VII. Proline *cis-trans* Isomerization Data Analysis

Both the single- and double-jump variants of the proline *cis-trans* isomerization kinetics experiments were run at temperatures of 278 (Figure S1) and 288 K (Figure 1c,d, Figure S2). For both temperatures, the intensities of the L13 and A15 peaks for monomers with P14 in the *cis* conformation were tracked over time. After a pressure drop, the *cis* population decreases, leading to a decaying exponential of the form:

$$I = I_0 e^{-k_{\text{ex}} t} + c$$

where  $k_{\text{ex}}$  is the P14 *cis-trans* isomerization exchange rate,  $I_0$  is the amplitude and  $c$  is the offset. A single time constant was globally fit for the exponential decay of both the L13<sub>*cis*</sub> and A15<sub>*cis*</sub> peaks in both the single- and double-jump datasets using the Matlab `nlinfit` function. The amplitude and offset were allowed to vary individually for both residues and both experiment variants. In the double-jump experiment, some fraction of the peptide reverts to the high-pressure equilibrium  $M_{\text{cis}}$  state during the readout HSQC, this percentage is always the same and simply results in an offset, or different fitted value of  $c$ , for the apparent  $M_{\text{cis}}$  concentration at equilibrium.

To determine how the P14 *cis-trans* isomerization rate,  $k_{\text{ex}}$ , partitions between the *cis-to-trans* rate constant,  $k_{\text{ct}}$ , and the *trans-to-cis* rate constant,  $k_{\text{tc}}$ , we determined the P14 *cis-to-trans* equilibrium constant,  $K_{\text{ct}}$ , at 288 K. This was done by comparing the integral of peaks corresponding to peptide with P14 in the *cis* and *trans* conformations for the pressure denatured peptide. At 288 K, P14 in the *cis* conformation makes up 11% of the monomeric peptide.<sup>11</sup> There is no pressure dependence for the P14 *cis* fraction of the unfolded monomer; hence, the amount of

unfolded, monomeric peptide is what controls the amount of peptide with P14 in the *cis* conformation.

### VIII. Pressure-jump & CPMG Relaxation Dispersion Global Fitting

Non-equilibrium kinetics of melittin with P14 in the *trans* conformation were numerically solved in Matlab with the ode23s solver using the following set of coupled ordinary differential equations to determine the populations of monomer,  $M_{trans}$ , dimer,  $D$ , and tetramer,  $T$ :<sup>12</sup>

$$\begin{aligned}\frac{d[M_{trans}]}{dt} &= -2k_2[M_{trans}]^2 + k_{-2}[D] \\ \frac{d[D]}{dt} &= 2k_2[M_{trans}]^2 - k_{-2}[D] - 2k_4[D]^2 + k_{-4}[T] \\ \frac{d[T]}{dt} &= 2k_4[D]^2 - k_{-4}[T]\end{aligned}$$

To fit the pressure-jump  $^{15}\text{N}$  stroboscopic chemical shift data, we first convert the populations to population-weighted average chemical shifts. The monomer and tetramer  $^{15}\text{N}$  chemical shifts were set to the assigned chemical shifts for these species. Although AlphaFold-Multimer<sup>13,14</sup> was unable to confidently predict dimer models (Figure S8), the SPARTA+ predicted backbone chemical shifts<sup>15</sup> for all dimer models (Figure S9) are similar to the experimentally observed  $^{15}\text{N}$  chemical shifts of the tetramer. Because the dimer population is very small (Figure 3b,c), we note that the derived  $k_2$  and  $k_{-4}$  rates are very insensitive to the  $^{15}\text{N}$  shifts of the dimeric intermediate. However, assigning chemical shifts of the disordered monomer to the dimer would increase both  $k_2$  and  $k_4$ , decreasing the population of the dimeric intermediate even further. During the 350-ms “unfold & dissociate” period a small fraction of the peptide does not unfold. With an unfolding rate of  $10\text{ s}^{-1}$  (Figure S5), 97% of the folded tetrameric protein unfolds during this delay, leading to a 3% underestimate of the folded tetramer population. The cosine and sine modulated components of the stroboscopic chemical shift evolution are calculated according to:

$$\begin{aligned}M_x(\tau) &= p_M \cos(\omega_{N,M}\kappa) + p_D \cos(\omega_{N,D}\kappa) + 1.03p_T \cos(\omega_{N,T}\kappa) \\ M_y(\tau) &= p_M \sin(\omega_{N,M}\kappa) + p_D \sin(\omega_{N,D}\kappa) + 1.03p_T \sin(\omega_{N,T}\kappa)\end{aligned}$$

where  $\kappa$  is the length of the chemical shift evolution period,  $p_M$ ,  $p_D$ , and  $p_T$  are fractional populations of the monomer, dimer, and tetramer, respectively, and  $\omega_{N,M}$ ,  $\omega_{N,D}$ ,  $\omega_{N,T}$  are the  $M_{trans}$ ,  $D$ , and  $T$  chemical shifts, respectively. The population-weighted average shifts are then given by:

$$\langle \delta_N(\tau) \rangle = \frac{1}{2\pi\kappa} \tan^{-1} \left( \frac{M_y(\tau)}{M_x(\tau)} \right)$$

In the limit where the stroboscopic chemical shift evolution period,  $\kappa$ , is much less than  $\pi/\Delta\omega_N$ , where  $\Delta\omega_N$  is the chemical shift difference between the unfolded and folded species, the population-weighted average shifts become a simple population-weighted average of the chemical shifts for  $M_{trans}$ ,  $D$ , and  $T$ :

$$\langle \delta_N(\tau) \rangle \approx p_M \delta_{N,M} + p_D \delta_{N,D} + 1.03p_T \delta_{N,T}$$

This simplified interpretation of the population weighted average shifts applies for all residues when  $\kappa = 0.5\text{ ms}$  and for residues with  $\frac{\Delta\omega_N}{2\pi} \ll 7.3\text{ ppm}$  when  $\kappa = 1.125\text{ ms}$ .

Analogous to how the population-weighted average chemical shifts are calculated according to the populations of  $M_{trans}$ ,  $D$ , and  $T$ , the population-weighted average chemical shifts were extracted from the stroboscopic chemical shift measurements according to:

$$\langle \delta_N(\tau) \rangle = \frac{1}{2\pi\kappa} \tan^{-1} \left( \frac{M_y(\tau)}{M_x(\tau)} \right)$$

where  $M_y(\tau)$  and  $M_x(\tau)$  are the sine- and cosine-modulated components collected during the pseudo-3D  $^{15}\text{N}$  stroboscopic chemical shift measurement. The error in the chemical shift measurements is then calculated according to:

$$\varepsilon(\tau) = \frac{N/|M(\tau)|}{\kappa}$$

where  $N$  is the noise level and  $|M(\tau)|$  is the magnitude of the  $M_y(\tau)$  and  $M_x(\tau)$  components.<sup>8</sup> Residues V5-T11, L13, A15, K17, S18, and I20 were included in these fits as these residues had sufficiently high signal to noise and a large enough chemical shift difference between the monomeric and tetrameric state to track appreciable chemical shift changes with respect to time (Figure S6). Residues V5-L9 have overlap between the  $M_{trans}$ ,  $M_{cis}$ , and  $M_{COOH}$  peaks in a  $^{15}\text{N}$ - $^1\text{H}$  HSQC spectrum. This manifests as an offset in the  $D$  and  $T$  chemical shifts for these residues in the fitting procedure described above. This was initially accounted for by scaling the  $D$  and  $T$  chemical shifts for residues V5-L9 such that the difference between the  $M$  and the  $D/T$  chemical shifts was 14%, which accounts for both the  $M_{cis}$  and small amount of  $M_{COOH}$  in the sample. Since  $M_{cis}$  makes up 11% of the sample at high pressure, this means that residual non-amidated melittin,  $M_{COOH}$ , makes up  $\sim 3\%$  of the sample. We note that the chemical shifts for the  $M_{cis}$  and  $M_{COOH}$  populations do not change over time in the stroboscopic chemical shift measurements, indicating that these populations are not in exchange with the  $M_{trans}$ ,  $D$ , or  $T$  populations on timescales relevant to these experiments. The average monomer populations from the first data points collected after the pressure drop were set as the initial conditions for the monomer population. The initial dimer population was set to 0.

In-phase  $^{15}\text{N}$  CPMG-RD curves were numerically calculated using Matlab by propagating the initial magnetization vector,  $M(0)$  according to:<sup>16</sup>

$$M(t) = (AA^*A^*A)^n M(0)$$

where  $M(0)$ , the initial magnetization vector, is equal to the equilibrium fractional populations of  $M_{trans}$ ,  $D$ , and  $T$ ,  $n$  is the number of CPMG cycles during the constant-time relaxation period, and  $A^*$  is the complex conjugate of the propagator,  $A$ . The equilibrium values were determined by numerically solving the kinetic rate equations for 100 seconds, which is much longer than the protein folding timescale. The propagator,  $A$ , is calculated using matrix exponentiation of the effective relaxation matrix,  $\tilde{R}$ .

$$A = e^{-\tilde{R}\tau_{CP}/2}$$

where  $\tau_{CP}$  is the time between successive  $180^\circ$  pulses.

The effective relaxation matrix,  $\tilde{R}$ , has contributions from chemical shift, intrinsic  $R_2$  relaxation, and chemical exchange:<sup>16</sup>

$$\tilde{R} = \tilde{R}^{CS} + \tilde{R}^{rel} + \tilde{R}^{ex}$$

where,

$$\tilde{R}^{CS} = i \begin{bmatrix} 0 & 0 & 0 \\ 0 & \Delta\omega^{dim} & 0 \\ 0 & 0 & \Delta\omega^{tetra} \end{bmatrix}$$

$$\tilde{R}^{rel} = \begin{bmatrix} R_2^{mon} & 0 & 0 \\ 0 & R_2^{dim} & 0 \\ 0 & 0 & R_2^{tetra} \end{bmatrix}$$

$$\tilde{R}^{ex} = \begin{bmatrix} k_2^{app} & -k_{-2} & 0 \\ -k_2^{app} & k_{-2} + k_4^{app} & -k_{-4} \\ 0 & -k_4^{app} & k_{-4} \end{bmatrix}$$

$k_2^{app}$  and  $k_4^{app}$  are calculated using the equilibrium concentrations of the monomer and dimer, respectively:<sup>12</sup>

$$k_2^{app} = 2k_2[M_{trans}]$$

$$k_4^{app} = 2k_4[D]$$

$R_{2,eff}$  relaxation rates are then extracted according to:

$$R_{2,eff} = \frac{-1}{t_{rel}} \ln \left( \frac{Re\{M(t)\}}{M(0)} \right)$$

where  $t_{rel}$  is the constant-time CPMG relaxation delay.

To fit the kinetic rate constants,  $k_2$ ,  $k_{-2}$ ,  $k_4$ , and  $k_{-4}$  to the data, the square of the residuals between the experimental and calculated stroboscopic  $^{15}\text{N}$  population weighted average chemical shifts, along with the experimental and calculated CPMG-RD  $R_{2,eff}$  relaxation rates, were minimized using the “fmincon” Matlab function. A scaling factor of 0.002 was multiplied by the square of the residuals for the CPMG-RD data so that the pressure-jump stroboscopic chemical shift measurement squared residuals and CPMG-RD squared residuals were of the same order of magnitude.

Prior to global fitting of both the pressure-jump stroboscopic chemical shift data and the CPMG-RD data,  $R_2^{mon}$ , was set to  $5 \text{ s}^{-1}$  for all residues,  $R_2^{dimer}$ , was set to  $10 \text{ s}^{-1}$  for all residues, and  $R_2^{tetra}$  was set to  $15 \text{ s}^{-1}$  for all residues. From the TROSY  $R_2$  measurements, we know that the tetramer dissociation constant,  $k_{-4}$ , is between 10 and  $20 \text{ s}^{-1}$ . A grid search was then performed to determine what order of magnitude of  $k_2$ ,  $k_{-2}$ , and  $k_4$  minimizes the squared residuals. The orders of magnitude found in this grid search were multiplied by the fitted rate constant parameters in subsequent fitting steps to ensure that the fitted parameters are of similar magnitude.

In the first round of global fitting, initial values of  $k_2$ ,  $k_{-2}$ ,  $k_4$ , and  $k_{-4}$ , were determined with the  $R_2$ 's and chemical shifts described above. The  $R_2$ 's for the monomer and tetramer were then fit by fixing the kinetic rate constants and minimizing the square of the residuals. The dimer  $R_2$ 's must be between values observed for the highly ordered tetramer and the highly disordered monomer and simply were set to the average of the monomer and tetramer  $R_2$ 's; the fits are insensitive to changes in these values and do not improve by allowing them to vary. Once the  $R_2$ 's were fit, the optimal effective chemical shifts were fit by fixing the kinetic rate constants and  $R_2$ 's and allowing the chemical shifts to vary by  $\pm 1.0$  ppm.

With the fitted  $R_2$ 's and effective  $^{15}\text{N}$  chemical shifts, we then globally fit the kinetic rate constants to the experimental pressure-jump and CPMG-RD data by minimizing the square of the

residuals between the experimental and calculated data points. Errors in the fitted kinetic rate constants,  $k_2$ ,  $k_{-2}$ ,  $k_4$ , and  $k_{-4}$ , were determined by taking the square roots of the diagonal elements of the inverse Hessian matrix, which is computed during the fitting procedure by the “fmincon” Matlab function.

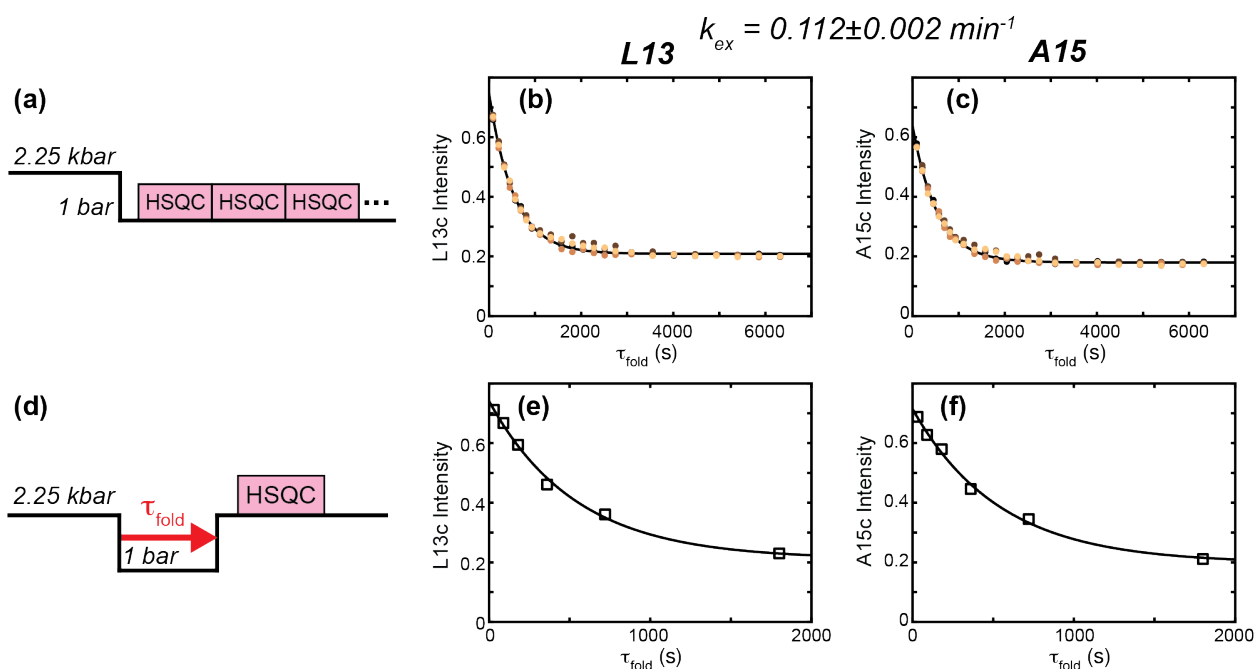


**Figure S1.** P14 *cis-trans* isomerization kinetics at 278 K of a 2 mM melittin sample. (a) Schematic representation of the experimental scheme employed where successive short HSQCs are collected after a pressure drop to atmospheric pressure. (b,c) Intensities of the (b) L13 and (c) A15 resonances corresponding to P14 in the *cis* conformation from the single-jump experiment. Different colors correspond to three repeats. Note that at 278 K, the single-jump scheme has plenty of temporal resolution to accurately quantify the proline *cis-trans* isomerization exchange. (d) Schematic representation of the double-jump proline *cis-trans* isomerization experiment. In this experiment, the pressure is dropped to atmospheric pressure for a variable delay,  $\tau_{\text{fold}}$ , before being jumped back up to denaturing conditions for a high-pressure readout HSQC. (e,f) Intensities of the (e) L13 and (f) A15 resonances corresponding to P14 in the *cis* conformation from the double-jump experiment.

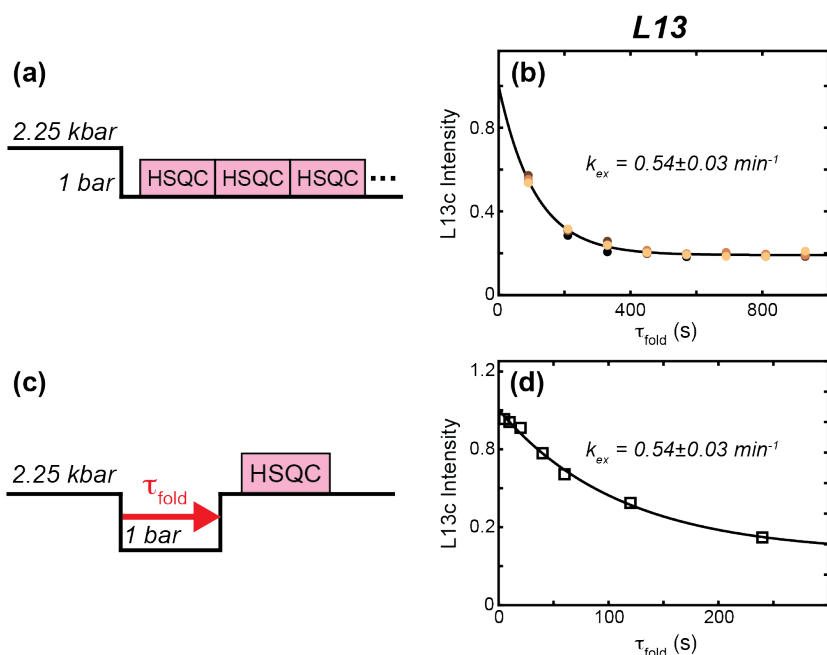


**Figure S2.** P14 *cis-trans* isomerization kinetics of 2 mM melittin at 288 K observed through L13. (a) Schematic representation of the experimental scheme employed where successive short HSQCs are collected after a pressure drop to atmospheric pressure. (b) Intensities of the L13 resonance corresponding to P14 in the *cis* conformation from the double-jump experiment. Colors represent results from 3 separate repeats. (c) Schematic representation of the double-jump proline *cis-trans* isomerization experiment. In this experiment, the pressure is dropped to atmospheric pressure for a variable delay,  $\tau_{\text{fold}}$ , before being jumped back up to denaturing conditions for a high-pressure readout HSQC. (d) Intensities of the L13 resonance corresponding to P14 in the *cis* conformation from the single-jump experiment.

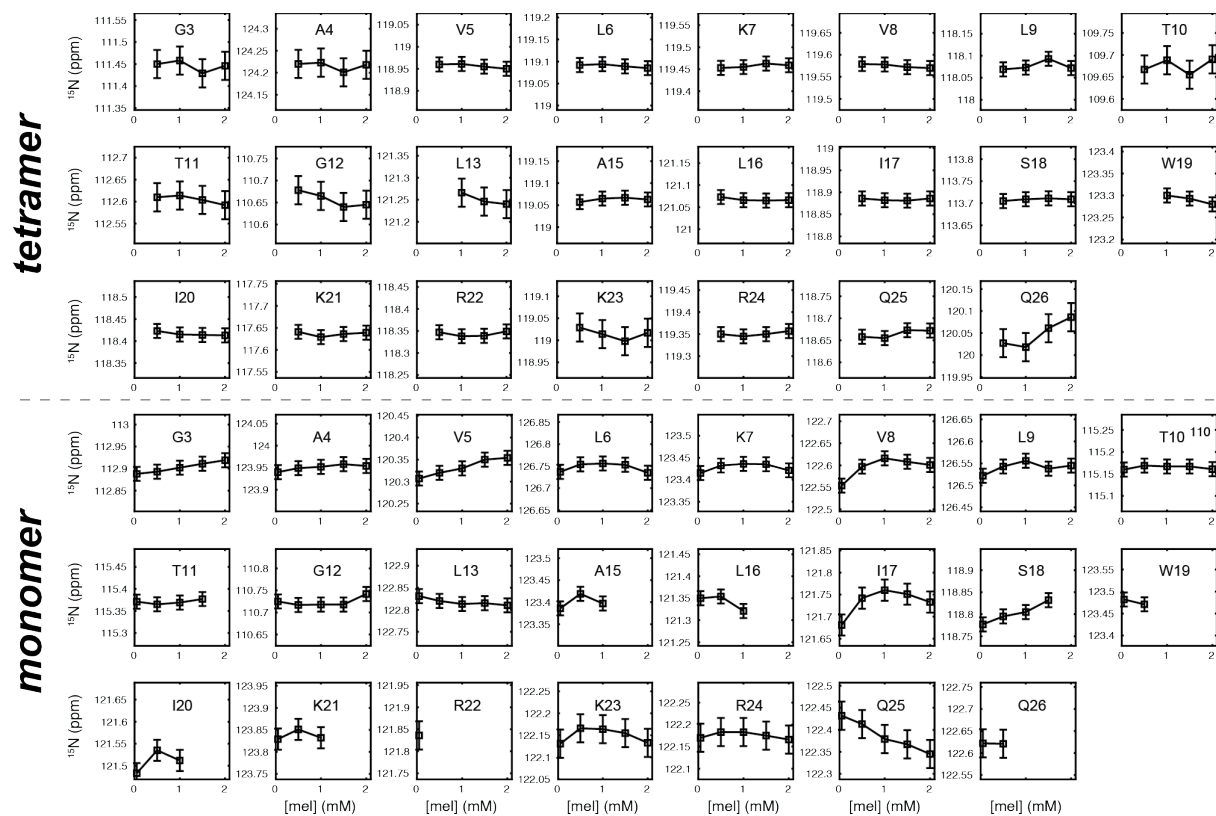


**Figure S3.**  $^{15}\text{N}$  chemical shift titration ranging from  $50\ \mu\text{M}$  to  $2\ \text{mM}$  of  $^2\text{H}$ ,  $^{13}\text{C}$ ,  $^{15}\text{N}$ -labeled melittin at  $288\ \text{K}$  to look for evidence of the dimer population exchanging with the monomer or tetramer populations. The lack of significant chemical shift changes with concentration indicates that the dimer population is either at a low level or has identical chemical shifts to the tetramer. Small chemical shift changes just outside of the error of the measurement were observed for several residues in the monomer (G3, A4, V5, and Q25 for example).

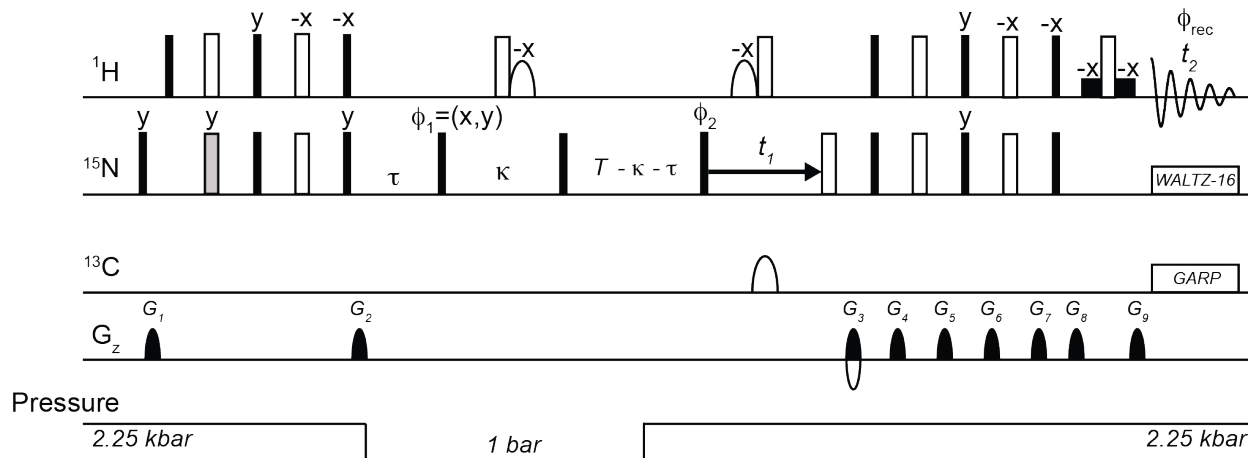


**Figure S4.** Pulse sequence for high-pressure readout pressure-jump pseudo-3D stroboscopic  $^{15}\text{N}$  chemical shift measurement under folding conditions.<sup>7</sup> After preparation at high pressure, where the peptide is equilibrated in the pressure-denatured state, a refocused INEPT generates in-phase  $\text{N}_z$  magnetization prior to a pressure drop to atmospheric pressure. Following the pressure drop, a variable folding delay,  $\tau_{\text{fold}}$ , precedes the stroboscopic chemical shift encoding. The pressure is then jumped back up to 2.25 kbar and the peptide is allowed to denature for a 350-ms “unfold & dissociate” period prior to evolving the indirect  $^{15}\text{N}$  dimension and INEPT transfer back to  $^1\text{H}$  for detection. Open rectangles represent hard  $180^\circ$  pulses, light gray rectangular pulses represent a composite  $180^\circ$  pulse ( $90^\circ_x 216^\circ_y 90^\circ_x$ ), tall black-filled rectangles represent hard  $90^\circ$  pulses, and short black-filled rectangles represent soft rectangular  $90^\circ$  pulses. The shaped pulses on the  $^1\text{H}$  channel correspond to 1.2-ms  $180^\circ$  water-flip-back pulses with an amplitude profile of the central lobe of a sinc function.<sup>17</sup> The shaped  $^{13}\text{C}$  pulse is a 700- $\mu\text{s}$  hyperbolic secant  $180^\circ$  pulse for decoupling during  $^{15}\text{N}$  evolution. Quadrature detection for the indirect  $t_1$  dimension was done using an echo-antiecho scheme<sup>9</sup> by inverting the encoding gradient,  $G_3$ , along with the phase of the first  $90^\circ$  on  $^{15}\text{N}$  following the  $t_1$  evolution. Phase cycling:  $\phi_1 = x, -x$ ;  $\phi_2 = x, x, -x, -x$ ,  $\phi_{\text{rec}} = x, -x, -x, x$ . Note that this phase cycling is for reading out the cosine-modulated signal; for reading out the sine modulated signal.  $\phi_1 = y, -y$ . Gradients along the  $z$  axis were sine-bell shaped with durations  $G_{1,2,3,4,5,6,7,8,9} = 1.9, 1.0, 2.0, 2.5, 2.5, 2.5, 2.5, 0.5,$  and  $0.296$  ms with  $z$ -gradient strengths of 51, 21, 47, 11, 11, 6, 6, -47, and -47 percent of the probe’s maximum gradient strength (*ca* 67 G/cm).

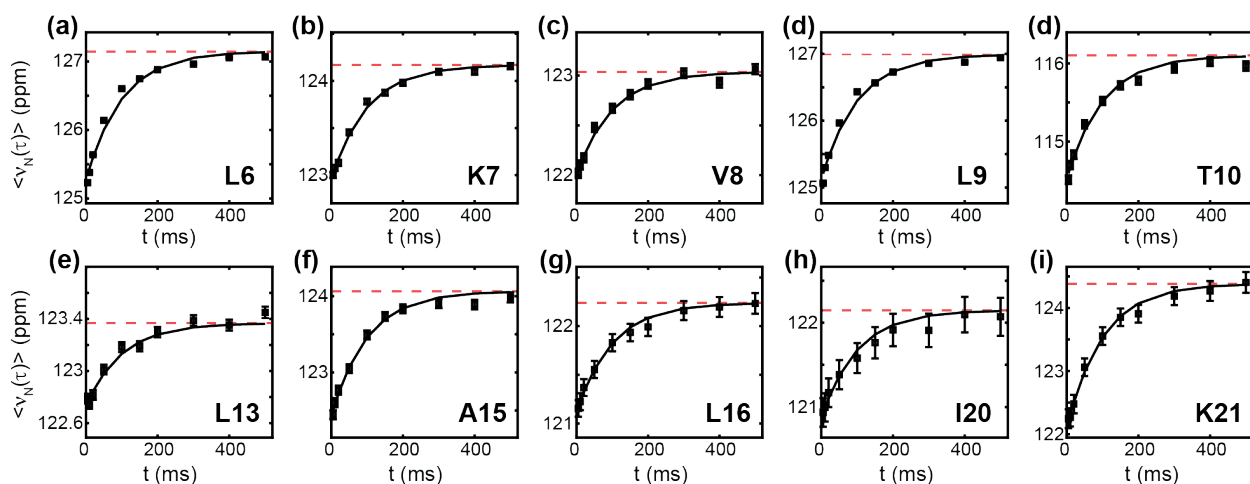


**Figure S5.** High-pressure readout pressure-jump pseudo-3D stroboscopic  $^{15}\text{N}$  chemical shift measurement under unfolding conditions. The pulse sequence used in this measurement was similar to Figure S4, but the sample equilibration and initial refocused INEPT transfer occurred at low pressure and were followed by a single pressure jump up to 2.25 kbar. These experiments were run on a 1.1 mM  $^2\text{H}$ ,  $^{13}\text{C}$ ,  $^{15}\text{N}$ -labeled melittin sample at 288 K. This experiment measured the rate of dissociation/unfolding under unfolding conditions. A global fit of the change in chemical shifts for the ten residues shown above yielded an unfolding time constant of  $100 \pm 8$  ms. Dashed red lines indicate the unfolded peaks'  $^{15}\text{N}$  chemical shifts in the high-pressure HSQC spectrum.

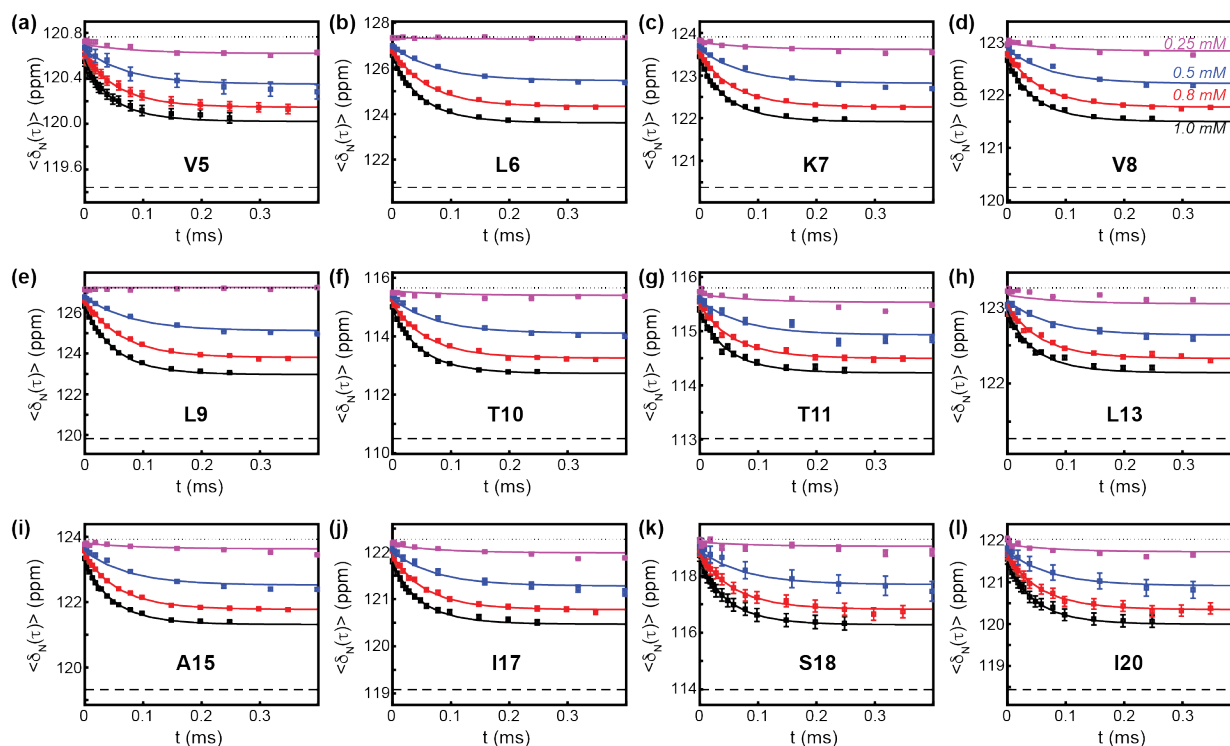


**Figure S6.** Pressure-jump pseudo-3D stroboscopic  $^{15}\text{N}$  chemical shift data under folding conditions for the 12 residues with well-defined, large chemical shift differences between folded and unfolded states, that were included in the  $M_{trans}$ -D-T model global fit together with the CPMG-RD data. Dashed and dotted black lines correspond to the  $^{15}\text{N}$  chemical shifts of the folded tetramer and unfolded monomer at 1 bar, respectively.

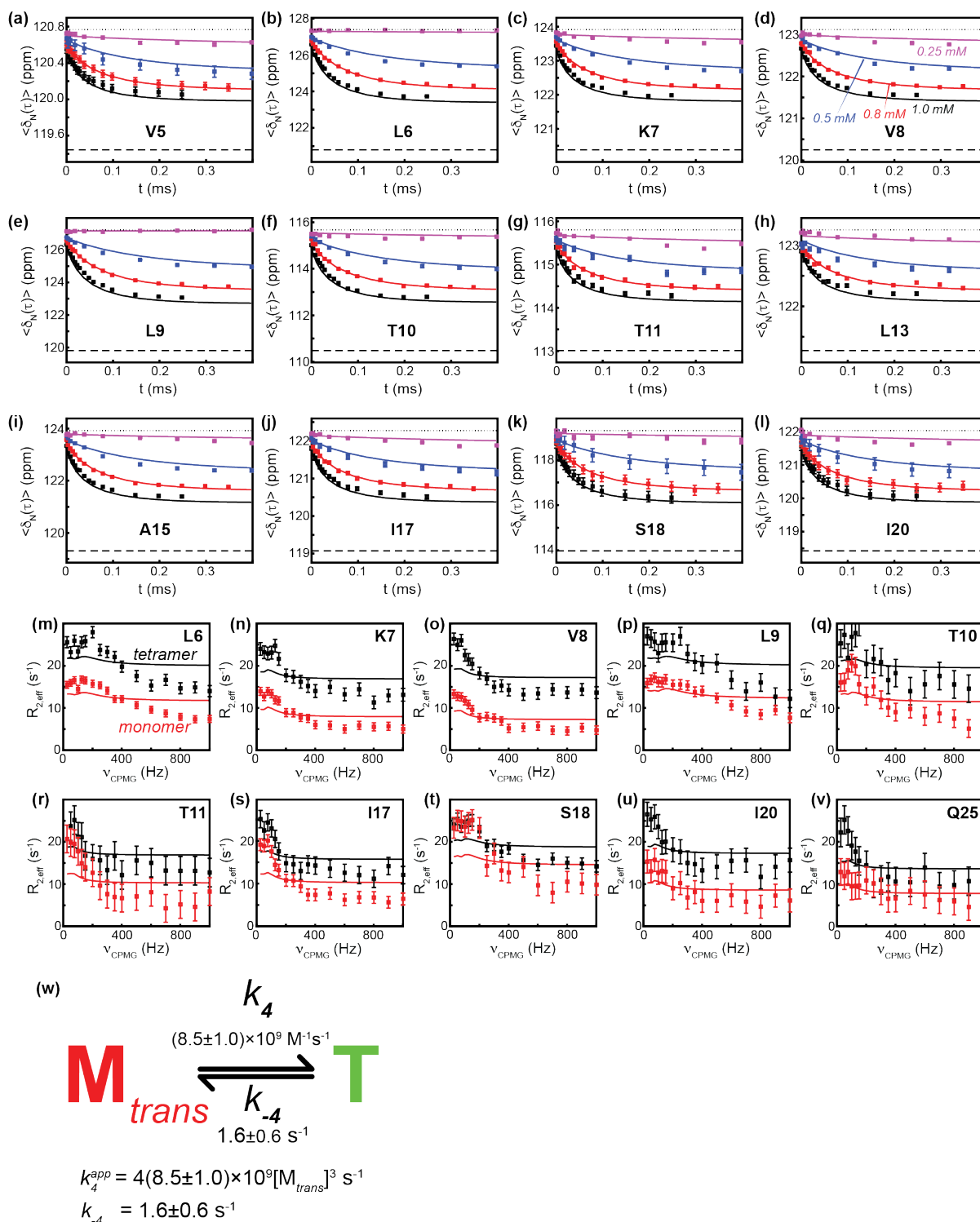


**Figure S7.** Tetramer model fits. Global fit to the pressure-jump and CPMG-RD assuming a simplified model in which an equilibrium of four monomers exchanging with one tetramer is considered. This model is equivalent to tetramer formation being rate limiting at all concentrations studied. (a-l) The pressure-jump data fits this model well, although discrepancies are observed for the 0.5 mM sample. (m-v) The CPMG-RD data fits poorly for this model. This model predicts much smaller dispersion than is observed for either the monomer or tetramer.

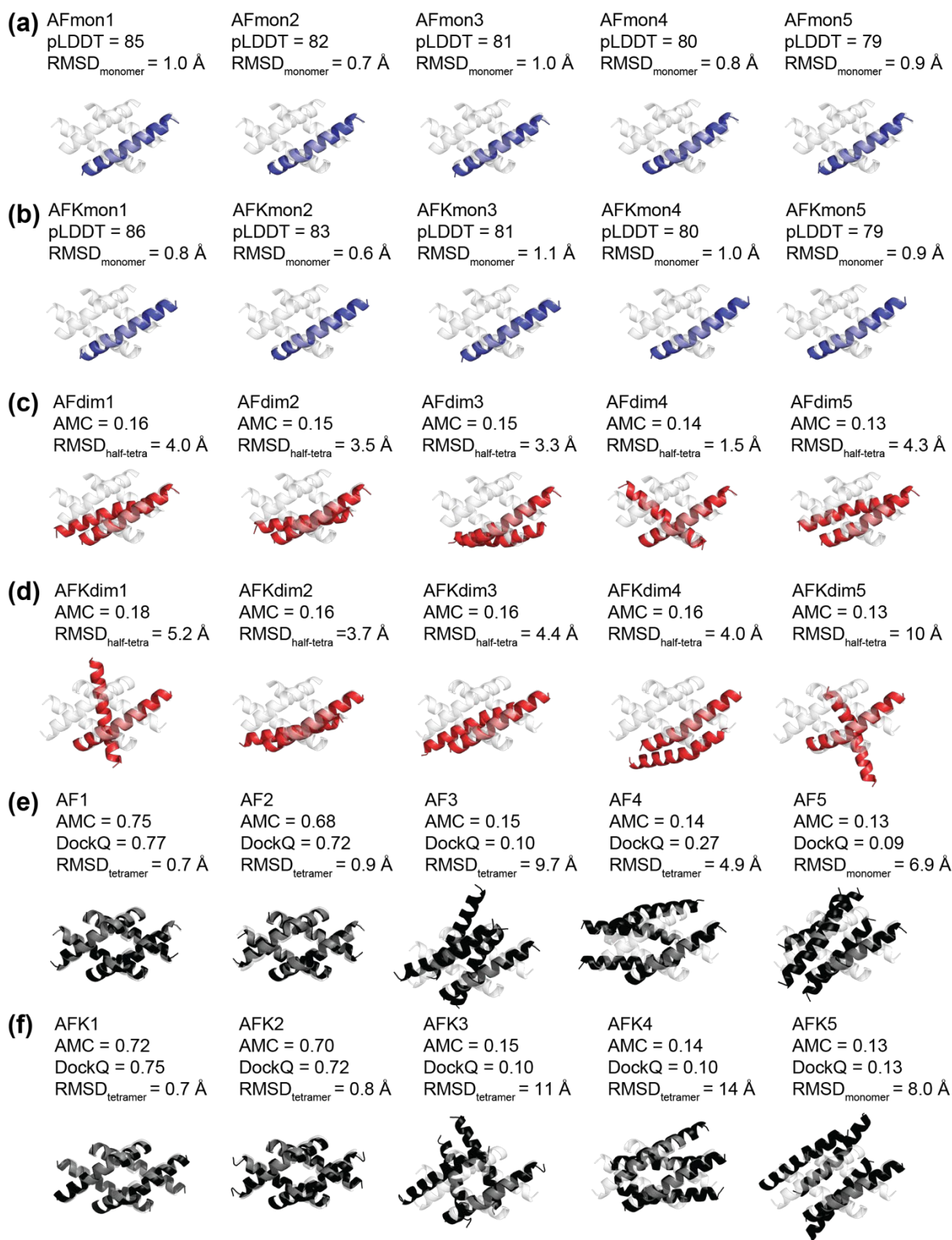


**Figure S8.** AlphaFold<sup>13,14</sup> structure predictions of the monomer, transient dimer, and stable tetramer. All structures were predicted in the same manner as previously described using a sequence-limited training database.<sup>2</sup> a), c) and e) depict structures predicted for the monomer,

dimer, and tetramer, respectively, containing the native melittin sequence but lacking the native C-terminal amidation, which is not supported by AlphaFold2. b), d), and f) depict structures predicted for the monomer, dimer, and tetramer, respectively, containing an additional C-terminal lysine residue to mitigate the negative charge of the C-terminal carboxylic acid. To visualize the similarity in monomer unit structures and the heterogeneity in interhelical packing, all structures have one monomer aligned with the x-ray crystal structure (PDB: 2MLT; displayed as a partially transparent white tetramer).<sup>18,19</sup> All of the predicted monomer subunits have nearly the same structure as the monomer subunit from the crystal structure, with backbone RMSDs of  $\sim 1$  Å or less. Backbone RMSDs for the predicted monomer structures with respect to the 2MLT crystal structure are shown in a) and b), for the predicted dimer structures with respect to the closest “half-tetramer” from the 2MLT crystal structure in c) and d), and for the predicted tetramer structures with respect to the 2MLT crystal structure in e) and f). The per-residue confidence estimates (pLDDT, ranging from 0 to 100) are a metric used by AlphaFold2 to predict its confidence in the predicted structure being the true structure.<sup>13</sup> None of the predicted dimer structures had AlphaFold-Multimer model confidence scores (AMC, defined as  $0.2 \cdot \text{pTM} + 0.8 \cdot \text{ipTM}$ , where the pTM and the ipTM are the predicted TM-score and the interface predicted TM-score<sup>14</sup>) above 0.18, indicating that these predicted models likely do not recapitulate the true quaternary structure of the transient dimer. DockQ scores<sup>20</sup> for the tetramers represent how well the predicted structure matches the 2MLT crystal structure. DockQ scores above 0.49 and 0.23 indicate medium and acceptable quality structures, respectively.

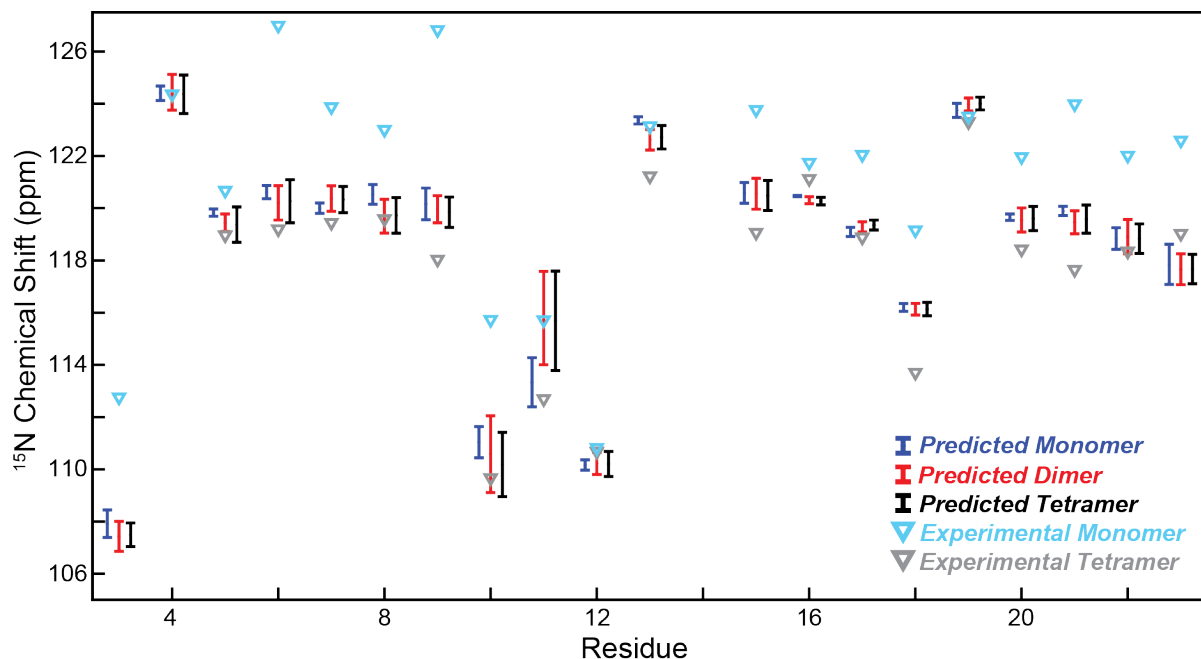


**Figure S9.** Experimental and predicted  $^{15}\text{N}$  backbone chemical shifts for the oligomeric states of melittin. Experimental monomer and tetramer shifts<sup>2</sup> are shown as light blue and gray triangles, respectively. Blue, red, and black error bars show the mean and standard deviation of the SPARTA+ predicted shifts<sup>15</sup> for the monomer, dimer, and tetramer. Although AlphaFold2 predicts a helical structure for the monomer, backbone chemical shifts clearly show that the monomer is in fact disordered.<sup>2</sup> It has previously been observed that AlphaFold2 often predicts helical segments for sequences even when there is experimental evidence for the sequence being intrinsically disordered.<sup>7,21–23</sup>

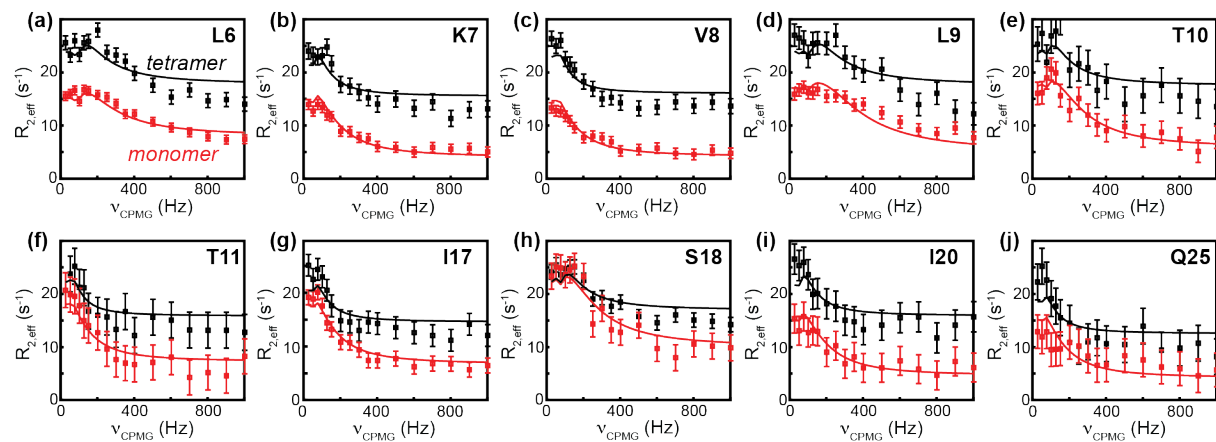


**Figure S10.** CPMG-RD data for the 10 residues included in the  $M_{trans}$ -D-T model global fit with the pressure-jump NMR data.

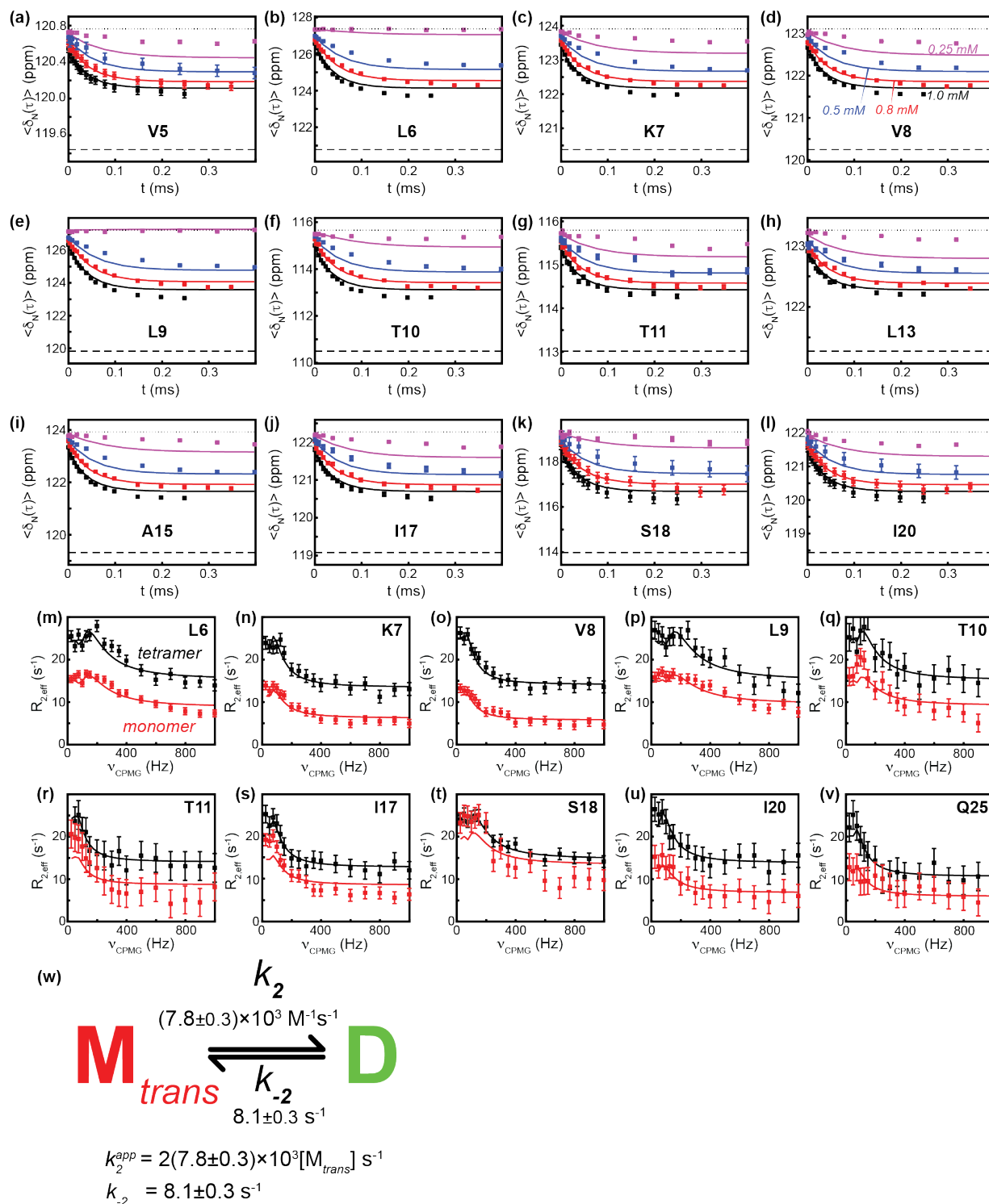


**Figure S11.** Global fit to the pressure-jump and CPMG-RD assuming a simplified model in which just the monomer to dimer equilibrium is considered. This model is equivalent to dimer formation being rate limiting at all concentrations studied. (a-l) The pressure-jump data clearly does not fit this model, particularly at the lower concentrations studied. (m-v) The CPMG-RD data is recapitulated quite well for most of the residues, although discrepancies are seen for some of the monomer curves, such as (t) S18.

**Table S1.**  $^{15}\text{N}$  TROSY  $R_2$  measurements for resonances corresponding to the tetramer in a 1.1 mM  $^2\text{H}$ ,  $^{13}\text{C}$ ,  $^{15}\text{N}$ -labeled melittin sample at 288 K.

Residue	500 MHz		700 MHz	
	$R_2$ ( $\text{s}^{-1}$ )	$R_2$ error ( $\text{s}^{-1}$ )	$R_2$ ( $\text{s}^{-1}$ )	$R_2$ error ( $\text{s}^{-1}$ )
V5	19.7	0.7	20.0	1.2
L6	20.7	0.4	20.9	1.3
K7	19.1	1.1	19.6	0.9
V8	19.8	0.7	20.4	0.4
L9	20.7	1.3	22.7	0.8
T10	24.4	2.8	28.5	2.7
T11	25.8	1.0	26.5	1.6
G12	18.3	1.1	21.6	1.4
L13	21.6	1.4	27.0	2.9
A15	17.7	0.4	17.9	0.8
L16	16.3	2.4	18.2	2.2
I17	19.4	0.6	18.2	0.6
S18	19.1	1.0	18.2	0.4
W19	14.1	1.6	16.2	1.8
I20	18.7	1.2	20.3	0.7
K21	19.2	0.8	18.5	0.4
R22	19.1	0.6	19.8	1.0
K23	20.5	0.4	22.3	0.5
R24	19.8	0.2	19.9	0.7
Q25	20.6	0.4	20.7	0.6
Q26	19.5	0.5	21.4	0.5

**Table S2.**  $^{15}\text{N}$  chemical shifts used in the global fit to the pressure-jump stroboscopic chemical shift measurements and CPMG-RD measurements.

Residue	Monomer (ppm)	Tetramer (ppm)
V5	120.77	119.44
L6	127.39	120.79
K7	123.91	120.38
V8	123.11	120.25
L9	127.22	119.82
T10	115.66	110.49
T11	115.80	113.01
L13	123.25	121.27
A15	123.92	119.32
I17	122.27	119.08
S18	119.30	113.98
I20	122.03	118.43
Q25	121.99	118.82

**Table S3.**  $R_{2,0}$  values used in fitting the CPMG-RD curves. The average of the monomer and tetramer  $R_{2,0}$  values was used for the dimer.

Residue	Monomer ( $s^{-1}$ )	Tetramer ( $s^{-1}$ )
L6	6.9	19.1
K7	3.5	16.9
V8	3.7	17.5
L9	4.3	19.2
T10	5.2	19.0
T11	7.1	16.9
I17	6.7	15.6
S18	9.9	17.8
I20	4.1	17.2
Q25	4.0	13.5

## References

- (1) Jeon, J.; Thurber, K. R.; Ghirlando, R.; Yau, W.-M.; Tycko, R. Application of Millisecond Time-Resolved Solid State NMR to the Kinetics and Mechanism of Melittin Self-Assembly. *Proc. Natl. Acad. Sci.* **2019**, *116* (34), 16717–16722. <https://doi.org/10.1073/pnas.1908006116>.
- (2) Gelenter, M. D.; Bax, A. Recombinant Expression and Chemical Amidation of Isotopically Labeled Native Melittin. *J. Am. Chem. Soc.* **2023**, *145* (7), 3850–3854. <https://doi.org/10.1021/jacs.2c12631>.
- (3) Charlier, C.; Alderson, T. R.; Courtney, J. M.; Ying, J.; Anfinrud, P.; Bax, A. Study of Protein Folding under Native Conditions by Rapidly Switching the Hydrostatic Pressure inside an NMR Sample Cell. *Proc. Natl. Acad. Sci.* **2018**, *115* (18), E4169–E4178. <https://doi.org/10.1073/pnas.1803642115>.
- (4) Wang, C.; Palmer III, A. G. Solution NMR Methods for Quantitative Identification of Chemical Exchange in <sup>15</sup>N-Labeled Proteins. *Magn. Reson. Chem.* **2003**, *41* (10), 866–876. <https://doi.org/10.1002/mrc.1262>.
- (5) Pervushin, K.; Riek, R.; Wider, G.; Wüthrich, K. Attenuated T<sub>2</sub> Relaxation by Mutual Cancellation of Dipole–Dipole Coupling and Chemical Shift Anisotropy Indicates an Avenue to NMR Structures of Very Large Biological Macromolecules in Solution. *Proc. Natl. Acad. Sci.* **1997**, *94* (23), 12366–12371. <https://doi.org/10.1073/pnas.94.23.12366>.
- (6) Delaglio, F.; Grzesiek, S.; Vuister, G. W.; Zhu, G.; Pfeifer, J.; Bax, A. NMRPipe: A Multidimensional Spectral Processing System Based on UNIX Pipes. *J. Biomol. NMR* **1995**, *6* (3), 277–293. <https://doi.org/10.1007/BF00197809>.
- (7) Chiliveri, S. C.; Shen, Y.; Baber, J. L.; Ying, J.; Sagar, V.; Wistow, G.; Anfinrud, P.; Bax, A. Experimental NOE, Chemical Shift, and Proline Isomerization Data Provide Detailed Insights into Amelotin Oligomerization. *J. Am. Chem. Soc.* **2023**, *145* (32), 18063–18074. <https://doi.org/10.1021/jacs.3c05710>.
- (8) Charlier, C.; Courtney, J. M.; Alderson, T. R.; Anfinrud, P.; Bax, A. Monitoring <sup>15</sup>N Chemical Shifts During Protein Folding by Pressure-Jump NMR. *J. Am. Chem. Soc.* **2018**, *140* (26), 8096–8099. <https://doi.org/10.1021/jacs.8b04833>.
- (9) Kay, L. E.; Keifer, P.; Saarinen, T. Pure Absorption Gradient Enhanced Heteronuclear Single Quantum Correlation Spectroscopy with Improved Sensitivity. *J. Am. Chem. Soc.* **1992**, *114* (26), 10663–10665. <https://doi.org/10.1021/ja00052a088>.
- (10) Hansen, D. F.; Vallurupalli, P.; Kay, L. E. An Improved <sup>15</sup>N Relaxation Dispersion Experiment for the Measurement of Millisecond Time-Scale Dynamics in Proteins. *J. Phys. Chem. B* **2008**, *112* (19), 5898–5904. <https://doi.org/10.1021/jp074793o>.
- (11) Alderson, T. R.; Lee, J. H.; Charlier, C.; Ying, J.; Bax, A. Propensity for Cis-Proline Formation in Unfolded Proteins. *ChemBioChem* **2018**, *19* (1), 37–42. <https://doi.org/10.1002/cbic.201700548>.
- (12) Rennella, E.; Sekhar, A.; Kay, L. E. Self-Assembly of Human Profilin-1 Detected by Carr-Purcell-Meiboom-Gill Nuclear Magnetic Resonance (CPMG NMR) Spectroscopy. *Biochemistry* **2017**, *56* (5), 692–703. <https://doi.org/10.1021/acs.biochem.6b01263>.
- (13) Jumper, J.; Evans, R.; Pritzel, A.; Green, T.; Figurnov, M.; Ronneberger, O.; Tunyasuvunakool, K.; Bates, R.; Židek, A.; Potapenko, A.; Bridgland, A.; Meyer, C.; Kohl,

- S. A. A.; Ballard, A. J.; Cowie, A.; Romera-Paredes, B.; Nikolov, S.; Jain, R.; Adler, J.; Back, T.; Petersen, S.; Reiman, D.; Clancy, E.; Zielinski, M.; Steinegger, M.; Pacholska, M.; Berghammer, T.; Bodenstein, S.; Silver, D.; Vinyals, O.; Senior, A. W.; Kavukcuoglu, K.; Kohli, P.; Hassabis, D. Highly Accurate Protein Structure Prediction with AlphaFold. *Nature* **2021**, *596* (7873), 583–589. <https://doi.org/10.1038/s41586-021-03819-2>.
- (14) Evans, R.; O'Neill, M.; Pritzel, A.; Antropova, N.; Senior, A.; Green, T.; Židek, A.; Bates, R.; Blackwell, S.; Yim, J.; Ronneberger, O.; Bodenstein, S.; Zielinski, M.; Bridgland, A.; Potapenko, A.; Cowie, A.; Tunyasuvunakool, K.; Jain, R.; Clancy, E.; Kohli, P.; Jumper, J.; Hassabis, D. Protein Complex Prediction with AlphaFold-Multimer. *bioRxiv* March 10, 2022, p 2021.10.04.463034. <https://doi.org/10.1101/2021.10.04.463034>.
- (15) Shen, Y.; Bax, A. SPARTA+: A Modest Improvement in Empirical NMR Chemical Shift Prediction by Means of an Artificial Neural Network. *J. Biomol. NMR* **2010**, *48* (1), 13–22. <https://doi.org/10.1007/s10858-010-9433-9>.
- (16) Kotler, S. A.; Tugarinov, V.; Schmidt, T.; Ceccon, A.; Libich, D. S.; Ghirlando, R.; Schwieters, C. D.; Clore, G. M. Probing Initial Transient Oligomerization Events Facilitating Huntingtin Fibril Nucleation at Atomic Resolution by Relaxation-Based NMR. *Proc. Natl. Acad. Sci.* **2019**, *116* (9), 3562–3571. <https://doi.org/10.1073/pnas.1821216116>.
- (17) Grzesiek, S.; Bax, A. The Importance of Not Saturating Water in Protein NMR. Application to Sensitivity Enhancement and NOE Measurements. *J. Am. Chem. Soc.* **1993**, *115* (26), 12593–12594. <https://doi.org/10.1021/ja00079a052>.
- (18) Terwilliger, T. C.; Eisenberg, D. The Structure of Melittin. I. Structure Determination and Partial Refinement. *J. Biol. Chem.* **1982**, *257* (11), 6010–6015. [https://doi.org/10.1016/S0021-9258\(20\)65097-9](https://doi.org/10.1016/S0021-9258(20)65097-9).
- (19) Terwilliger, T. C.; Eisenberg, D. The Structure of Melittin. II. Interpretation of the Structure. *J. Biol. Chem.* **1982**, *257* (11), 6016–6022. [https://doi.org/10.1016/S0021-9258\(20\)65098-0](https://doi.org/10.1016/S0021-9258(20)65098-0).
- (20) Basu, S.; Wallner, B. DockQ: A Quality Measure for Protein-Protein Docking Models. *PLOS ONE* **2016**, *11* (8), e0161879. <https://doi.org/10.1371/journal.pone.0161879>.
- (21) Laurents, D. V. AlphaFold 2 and NMR Spectroscopy: Partners to Understand Protein Structure, Dynamics and Function. *Front. Mol. Biosci.* **2022**, *9*.
- (22) Ruff, K. M.; Pappu, R. V. AlphaFold and Implications for Intrinsically Disordered Proteins. *J. Mol. Biol.* **2021**, *433* (20), 167208. <https://doi.org/10.1016/j.jmb.2021.167208>.
- (23) Pinheiro, F.; Santos, J.; Ventura, S. AlphaFold and the Amyloid Landscape. *J. Mol. Biol.* **2021**, *433* (20), 167059. <https://doi.org/10.1016/j.jmb.2021.167059>.